Catalysis Science & Technology

PAPER

View Article Online
View Journal | View Issue

Cite this: *Catal. Sci. Technol.*, 2017, 7, 5882

Investigation of methanol conversion over high-Si beta zeolites and the reaction mechanism of their high propene selectivity†

Xuebin Zhao,[abc] Linying Wang,[a] Jinzhe Li,[a] Shutao Xu,[a] Wenna Zhang,[ab] Yingxu Wei,[a] Xinwen Guo,[c] Peng Tian*[a] and Zhongmin Liu*[a]

Received 1st September 2017,
Accepted 8th November 2017

DOI: 10.1039/c7cy01804e

rsc.li/catalysis

Large pore high-Si beta zeolites (Si/Al = 136 to 340) were synthesized by a HF-assisted method, and their catalytic performance for the conversion of methanol to propene was explored. It is demonstrated that beta zeolites with low acid density facilitate the achievement of high propene selectivity and a high propene/ethene ratio. The HF dosage in the synthesis has great influence on the Al distribution in the framework, as evidenced by ^{27}Al MAS NMR and ^{27}Al MQ MAS NMR spectroscopy, which may influence the acidity and microstructure of acid sites and lead to a remarkable catalytic lifespan. A HF/SiO_2 ratio of 0.45 is found to facilitate the synthesis of high-Si beta enriched with Al atoms located at the T9 sites; this helps the catalyst show the longest lifetime, with a propene selectivity of 49.7–58.3% at 550 °C and WHSV = 2 h^{-1}. With the aid of $^{12}C/^{13}C$-methanol switch experiments, we elucidated that the olefin-based mechanism dominates the reaction and contributes to the formation of ethene, propene, and higher olefins. Moreover, two phenol compounds are identified in the coke species, which have not been observed previously and have been found to be detrimental to the reaction.

1. Introduction

Light olefins are important raw materials for the petrochemical industry; the demand for these olefins has been increasing for several decades. Traditionally, light olefins are produced by steam cracking of naphtha and fluid catalytic cracking. The development of methanol-to-olefins processes has opened an alternative route to produce light olefins and has aroused significant interest in both the academic and industrial fields because the use of methanol as a starting material can reduce the dependence on petroleum resources. Currently, several processes have been commercialized including DICP methanol-to-olefins (DMTO) process,[1–3] UOP/hydro methanol-to-olefins process[4,5] and Lurgi's methanol-to-propene (MTP) process.[6] Both MTO processes use small pore SAPO-34 as the catalyst, and the MTP process is based on a medium pore ZSM-5 catalyst.

With the aim of developing more selective catalysts for methanol conversion and realizing product selectivity control, great efforts have been dedicated towards understanding the methanol conversion mechanism. It is generally accepted that the reaction follows an indirect pathway in which two catalytic cycles may be involved, that is, the aromatic-based hydrocarbon pool (HCP) mechanism and the olefins methylation and cracking mechanism.[7–10] In the aromatic-based cycle, methylbenzenes, methylcyclopentadienes, and their corresponding carbenium cations have been revealed to be the active HCP species, in which methylbenzenes with two or three methyl groups preferentially yield ethene, whereas higher methylbenzenes facilitate the formation of propene and butene.[11–13] In the olefin-based cycle, higher olefins formed by the methylation of light olefins are reactive intermediates, and ethene is demonstrated to be a minor cracking product from the olefins, in contrast to propene and butene.[10,14,15] Both catalytic cycles are interconnected by the secondary reaction of higher olefins to methylbenzenes, such as oligomerization, cyclization and hydrogen transfer.

Zeolite topology can exert influence on the reaction mechanisms and product selectivity of these processes. For example, our previous work[16,17] showed that over cavity-type SAPO/zeolites with 8-membered ring (MR) pores, the aromatic mechanism is generally effective for the reaction due to the

[a] *National Engineering Laboratory for Methanol to Olefins, Dalian National Laboratory for Clean Energy, Dalian Institute of Chemical Physics, Chinese Academy of Sciences, Dalian 116023, P.R. China. E-mail: tianpeng@dicp.ac.cn, liuzm@dicp.ac.cn; Fax: +86 411 84379289; Tel: +86 411 84379998*
[b] *University of Chinese Academy of Sciences, Beijing 100049, P. R. China*
[c] *State Key Laboratory of Fine Chemicals, PSU-DUT Joint Center for Energy Research, School of Chemical Engineering, Dalian University of Technology, Dalian 116024, P.R. China*

† Electronic supplementary information (ESI) available: More details of the experiment, additional XRD patterns, SEM, ^{27}Al MAS NMR, NH_3-TPD and porous properties of samples. See DOI: 10.1039/c7cy01804e

ready formation of HCP species in the supercages. Although the detailed HCP species differ with the cavity size, ethene and propene are observed to be the main products because of the diffusion limitation of higher olefins imposed by the small apertures. On the other hand, for zeolites with only one dimension (1D) 10-MR channels, such as ZSM-22 and SAPO-41, the olefins-based route is dominant in the reaction, with propene, butene and C_{5+} as the main products, due to the insufficient space for the formation of aromatics intermediates.[18–21] Poor catalytic stability was always observed with these zeolites due to the mass transfer limitation in the 1D channels. Moreover, both catalytic cycles can coexist in the reaction (dual-cycle mechanism) over large pore 12-MR zeolites and medium pore zeolites with interconnected 10-MR channels.[22–25] This was first proposed based on studies of the reaction over ZSM-5 by Bjørgen *et al.*;[10] over this catalyst, lower methylbenzenes were found to be more active due to the smaller channel intersections, contributing to the formation of ethene. The formation of C_{3+} olefins arises from the olefin methylation and cracking route.

In addition to their topology, the acidity of zeolites also plays an important role in the formation of intermediates and the generation of light olefins.[26–29] A higher concentration of Brønsted acid sites will prompt side reactions and reduce the lifetime and light olefins selectivity of the catalyst.[30–33] Moreover, Olsbye *et al.*[27] investigated the reaction over SAPO-5 and SSZ-24, both of which have the same AFI topology with 1D 12-MR channels. They found that the moderately acidic SAPO-5 favors an olefin-mediated reaction mechanism with C_3–C_5 olefins as the main products. The strongly acidic H-SSZ-24 is more selective towards aromatic products and C_2–C_3 hydrocarbons. These results suggest that weaker acid strength facilitates the olefins-based cycle. Acid strength and acid concentration can be important design parameters for selectivity optimization in zeotype catalysis.

To date, catalyst development for the MTP process has mainly focused on small and medium pore zeolites based on the consideration of shape-selectivity control. A propene selectivity of 40% to 50% with a propene/ethene ratio of 5 to 10 has been achieved over ZSM-5 by carefully controlling the acidity, morphology and size of the catalyst.[34–36] Note that a higher propene/ethene ratio is desirable for the commercial MTP process due to the reduced energy consumption for the separation of gas products. However, one recent study by Tatsumi *et al.* indicates that a CON-type Al-containing borosilicate zeolite (Si/Al = 100 to 200) which consists of a 3D pore system with 12-, 12-, and 10-MR channels and is prepared using trimethyl-(−)-*cis*-myrtanylammonium hydroxide as the organic template shows high propene selectivity and low ethene selectivity in methanol conversion.[37] This work implies that large pore zeolites may produce propene and higher olefins with high selectivity if the acid properties of the zeolites are carefully modulated. Given that weaker acidity and lower acid concentration of zeolites facilitate the suppression of the aromatization of olefin products in the methanol reaction, it is envisioned that large pore zeolites with high Si/Al ratios and weak acid strengths may demonstrate interesting performance for propene production.

Among large pore zeolites, beta is an interesting candidate because of its relatively weak acidity and 3D pore system.[38] Previous studies have shown that beta with a low Si/Al ratio is active for methanol conversion, with a large amount of aromatic products.[39,40] The reaction temperature was generally controlled to be lower than 350 °C to better examine the reaction mechanism.[41] Also, the aromatics-based cycle was revealed to greatly contribute to the reaction, with hexamethylbenzene and heptamethylbenzenium cation as the active HCP species. Further, Bjørgen *et al.*[23] studied the reaction over beta zeolite with a Si/Al ratio of 120 at 350 °C and achieved a high propene/ethene ratio of 21 with a propene selectivity of 22.7%. A dual cycle mechanism was found to function in the reaction. Recently, Zhang *et al.*[42] also showed that beta catalyst (Si/Al = 120) can produce more propene during methanol conversion. Moreover, Yokoi *et al.*[43] developed a post-synthetic dealumination method to increase the Si/Al ratio of beta zeolites and achieved 37.4% to 49.7% propene selectivity over dealuminated beta with a Si/Al ratio of 112. These studies suggest that beta zeolites with increased Si/Al ratios can present interesting catalytic performance for the MTP reaction.

Herein, high-Si beta zeolites with varying Si/Al ratios (Si/Al = 130 to 340) were synthesized with the assistance of fluoride ion, and their catalytic performance in methanol conversion was investigated. In an attempt to achieve high propene selectivity, low ethene selectivity and long catalytic lifespan, the influence of the initial HF/SiO_2 ratios, zeolite Si/Al ratios and reaction conditions were examined in detail. Using the $^{12}C/^{13}C$-methanol switch technique, a reaction mechanism was proposed to elucidate the origin of the high propene selectivity over high-Si beta (Si/Al ≈ 280) at high temperature (450 °C to 550 °C). Moreover, solid-state MAS NMR, NH_3-TPD and coke species analysis were also performed to better understand the remarkable catalytic lifespans and product selectivities of the samples.

2. Experimental

2.1. Synthesis of beta zeolites

The chemical reagents used for the syntheses include: tetraethoxysilane (TEOS, Tianjin Kemiou Chemical Reagent Co), tetraethylammonium hydroxide (TEAOH, 35 wt%, Tianjin Damao Chemical Co), $Al(NO_3)_3{\cdot}9H_2O$ (Tianjin Kemiou Chemical Reagent Co), and hydrofluoric acid solution (40 wt%, Tianjin Damao Chemical Co). Typical synthesis of beta zeolites is as follows: 31.56 g TEAOH solution was added to 31.25 g TEOS under stirring. After 2 h, 0.188 g $Al(NO_3)_3{\cdot}9H_2O$ dissolved in 4.0 g water was mixed with the above clear solution and stirred for 0.5 h. Subsequently, 4.5 g 40 wt% HF solution was quickly added to the solution. The excess water was evaporated at 60 °C to afford a final gel with a molar composition of $1SiO_2 : 1/600Al_2O_3 : 0.5TEAOH : 0.6HF : 3H_2O$.

The final gel was transferred into a Teflon-lined stainless steel autoclave. Crystallization was carried out at 160 °C under tumbling at 60 rpm. After 12 h of crystallization, the slurry was centrifuged, washed with distilled water, and dried at 120 °C for 12 h. The organic template in the product was removed by calcination at 550 °C for 4 h. The solid yield of the product was calculated on the basis of SiO_2. The samples were named B*x*-*y*, where *x* represents the Si/Al ratio in the gel and *y* refers to the HF/SiO_2 ratio.

2.2. Characterization

Powder XRD patterns were recorded on a PANalytical X'Pert PRO X-ray diffractometer with Cu-Kα radiation (λ = 0.15418 nm), operating at 40 kV and 40 mA. The chemical compositions of the solid samples were determined with a PhilipsMagix-601 X-ray fluorescence (XRF) spectrometer. The crystal morphologies were observed using a scanning electron microscope (Hitachi SU8020). N_2 adsorption–desorption isotherms at −196 °C were determined on a Micromeritics ASAP2020 instrument. Prior to the measurements, the samples were degassed at 350 °C under vacuum for 4 h. The total surface areas were calculated based on the BET equation. The micropore volume and micropore surface area were evaluated using the *t*-plot method. All solid state NMR experiments were performed using a Bruker Avance III 600 spectrometer equipped with a 14.1 T wide-bore magnet. The resonance frequencies in this field strength were 150.9 and 119.2 MHz for ^{27}Al and ^{29}Si, respectively. The ^{29}Si MAS NMR spectra were recorded at a spinning rate of 8 kHz using high-power proton decoupling. 1024 scans were accumulated, with a $\pi/4$ pulse width of 2.5 μs and a 10 s recycle delay. Chemical shifts were referenced to 4,4-dimethyl-4-silapentane sulfonate sodium salt (DSS). ^{27}Al MAS NMR spectra were recorded at a spinning rate of 12 kHz using one pulse sequence. 200 scans were accumulated, with a $\pi/8$ pulse width of 0.75 μs and a 2 s recycle delay. Chemical shifts were referenced to $(NH_4)Al(SO_4)_2{\cdot}12H_2O$ at −0.4 ppm. Two-dimensional (2D) ^{27}Al MQ MAS NMR experiments were performed at a spinning speed of 12 kHz. An rf field of 200 kHz was used for the creation (0Q → ±3Q) and the first conversion (±3Q → 0Q) pulses. An rf field of 10 kHz was used for the last conversion step (0Q → ±1Q), which was the central transition selective soft 90° pulse. A two-dimensional (2D) Fourier transformation followed by a shearing transformation provided a pure absorption mode 2D contour plot.[44–46] The isotropic chemical shift (δ_{iso}) values were calculated according to literature procedures.[46] Temperature-programmed desorption of ammonia (NH_3-TPD) was measured on a Micrometric 2920 chemical adsorption instrument. Each sample (40 to 60 mesh, 0.20 g) was loaded into a quartz U-shaped reactor and pretreated at 600 °C for 1 h in flowing He. After the pretreatment, the sample was cooled to 100 °C and saturated with NH_3 gas. Then, NH_3-TPD was carried out in a constant flow of He (20 mL min^{-1}) from 100 °C to 550 °C at a heating rate of 10 °C min^{-1}.

2.3. Catalytic reaction

0.3 g calcined catalyst was pressed, sieved to 40 to 60 mesh and loaded in a fixed-bed quartz tubular reactor with an inner diameter of 8 mm. Prior to the reaction, the catalyst was activated at 550 °C for 60 min; then, the temperature was adjusted to the reaction temperature. Methanol was fed by passing the carrier gas (40.0 mL min^{-1}) through a saturator containing methanol at 35 °C, which afforded a WHSV of 4.0 h^{-1}. Methanol conversion was performed under atmospheric pressure. The effluent products from the reactor were maintained at 200 °C and analyzed by an online Agilent 7890A GC equipped with a PONA capillary column (100 m × 0.25 mm × 0.5 μm) and a FID detector. The conversion and selectivity were calculated on the basis of CH_2. Dimethyl ether (DME) was considered to be a reactant in the calculation.

2.4. Coke species analysis

After the reaction, the catalyst was discharged and placed in a vessel containing liquid nitrogen. 100 mg spent sample was transferred into a Teflon vial and treated with 1 mL dichloromethane (10 ppm C_2Cl_6 as internal standard) under ultrasound for 30 min to extract the surface organic species; then, the organic phase was separated. Subsequently, after washing three times with dichloromethane, the sample was dissolved in 1 mL 40% HF solution. The residual organic species in the catalyst micropore were further extracted using 1 mL dichloromethane with 10 ppm C_2Cl_6. The organic species were analyzed by GC-MS (Agilent 7890A/5975C MSD) with an HP-5 MS capillary column (30 m × 0.25 mm × 0.25 mm).

2.5. ^{12}C/^{13}C-methanol switch experiments

In the ^{12}C/^{13}C-methanol switch experiments, after ^{12}C-methanol was fed for 30 min at 550 °C and WSHV = 4.0 h^{-1}, the methanol feed was stopped and the feeding line was switched to ^{13}C-methanol for a further 30 s; the effluent products from the reactor were kept warm and analyzed by an online gas chromatograph (GC) equipped with a PoraPLOT-Q capillary column, an FID detector and a mass spectrometric detector (Agilent 7890B/5977A). Meanwhile, the off-gas was collected by CH_2Cl_2 every 10 s to better detect the aromatic products; for example, for the 30 s data, the off-gas from 25 s to 35 s was collected. The CH_2Cl_2 solutions were analyzed by GC-MS (Agilent 7890A/5975C MSD) with a HP-5 MS capillary column.

3. Results and discussion

3.1. Synthesis of high-Si beta zeolites with varying Si/Al ratios and their catalytic performance in methanol conversion

High-Si beta zeolites with different Si/Al ratios were synthesized in fluoride media. The detailed synthetic conditions and product compositions are listed in Table 1, and the XRD patterns of the samples are shown in Fig. S1.† All the samples show typical diffraction patterns of beta zeolite, with the

Table 1 The Si/Al ratios, solid yields and acid densities of the products[a]

Sample	B150-0.60	B200-0.60	B250-0.60	B300-0.60	B350-0.60	B400-0.60
Si/Al ratio in gel	150	200	250	300	350	400
Si/Al ratio in product[b]	136	167	206	278	314	340
Product yield (wt%)	84.7	84.0	86.8	89.8	89.0	86.6
D_{acid} (mmol g^{-1})[c]	0.078	0.070	0.056	0.047	0.042	0.040

[a] Initial gel molar composition: $SiO_2 : Al_2O_3 : TEAOH : HF : H_2O = 1 : 1/2x : 0.5 : 0.6 : 3$ (160 °C, 12 h). [b] Determined by XRF. [c] Acid density determined by NH_3-TPD.

coexistence of sharp and broad reflections corresponding to the *BEA structure, which mainly consists of polymorphs A and B with stacking disorder. The Si/Al ratios of the products determined by XRF are slightly lower than those of the gels, which is consistent with their high solid yields of above 84.0%. The SEM images of the samples are displayed in Fig. S2;† the images show that all the beta crystals are of micrometer size, but their particle sizes are not uniform. NH_3-TPD experiments were carried out to probe the acid properties of the samples, and the curves are given in Fig. S3.† Two distinct desorption peaks are present, centered around 160 °C and 330 °C; these peaks correspond to weak and strong acid sites, respectively, on the samples. Given that the acid amount of the high-Si samples is low and the crystal sizes of the samples are in a similar range, herein the small change in NH_3 desorption temperature for all the high-Si beta samples suggests their similar acid strengths. The acid densities of the samples are summarized in Table 1. A gradual decrease of acid sties can be observed with increasing Si/Al ratio.

Catalytic tests of methanol conversion were carried out at 500 °C in a fixed-bed reactor over high-Si beta zeolites with different Si/Al ratios, and the results are given in Table 2. The catalytic lifespan of the samples varies with the Si/Al ratio, and longer lifespans were observed over the B200-0.60, B250-0.60 and B300-0.60 samples. Further increasing the Si/Al ratio (catalysts B350-0.60 and B400-0.60) results in reduced catalytic stability, which is likely due to insufficient acid sites. Interestingly, for all samples, propene is the dominant product, reaching a selectivity of 43.3% to 48.9%; this indicates that high-Si beta catalysts are very selective for the production of propene from methanol. The results are distinct from those over low-Si beta[40] and show obviously improved catalytic performance. As the zeolite Si/Al ratio increases, the selectivities to propene, butene and long-chain hydrocarbons of $C_{5+}{}^N$ display a rising trend, while the formation of $C_{1-4}{}^0$, ethene and aromatics is depressed. The corresponding propene/ethene ratio rises with increasing Si/Al ratio; a maximum value of 18.5 is observed over B400-0.60, which has the lowest acid density. Moreover, the hydrogen transfer index (HTI), which reflects the hydrogen transfer level of the secondary transformation of olefin products, was calculated herein to evaluate the side reactions in the methanol conversion. From Table 2, the HTI value based on the selectivity ratio of butane to butene displays a monotonous decreasing trend with increasing Si/Al ratio. Given the descending acid concentration from catalysts B150-0.60 to B400-0.60, weakened hydrogen transfer ability can be clearly observed, which is in good agreement with the increased selectivity to olefin products. On the other hand, it is inferred from the decreased aromatics selectivity and increased $C_{5+}{}^N$ selectivity from B150-0.60 to B400-0.60 that the olefin-based catalytic cycle may increasingly dominate the aromatic-based cycle with the decreasing catalyst acid concentration.

3.2. Synthesis and characterization of high-Si beta with different HF/SiO_2 ratios

The effects of HF concentration in the initial gel on the synthesis were examined, considering that HF as a mineralizer is essential to the crystallization of high-Si beta and may have effects on the crystallinity, microstructure and catalytic performance of the products. Herein, the synthetic system of sample B300-0.60 with an initial Si/Al ratio of 300 was chosen

Table 2 Product distributions of methanol conversion over high-Si beta zeolites with different Si/Al ratios[a]

Sample	Lifetime (h)	Selectivity[b] (wt%)							
		$C_{1-4}{}^0$	C_2H_4	C_3H_6	C_4H_8	$C_{5+}{}^N$	Aro	C_3H_6/C_2H_4	HTI[c]
B150-0.60	2.2	9.1	4.2	43.3	18.8	11.6	13.0	10.3	0.31
B200-0.60	3.6	7.0	3.9	46.5	21.2	11.7	10.8	11.9	0.21
B250-0.60	3.6	5.4	3.3	48.5	22.3	12.8	9.1	14.7	0.16
B300-0.60	3.6	4.7	3.3	48.5	22.9	12.9	7.6	14.7	0.13
B350-0.60	2.2	3.9	3.0	48.9	23.1	13.9	6.9	16.3	0.11
B400-0.60	1.5	3.7	2.6	48.1	22.5	15.3	6.7	18.5	0.10

[a] Reaction conditions: 500 °C, WSHV = 4.0 h^{-1}. The lifetime is defined as methanol conversion above 99%. [b] The selectivity data at TOS = 47 min. $C_{1-4}{}^0$: alkanes with carbon numbers from 1 to 4, $C_{5+}{}^N$: non-aromatic products with carbon numbers greater than 4, Aro: aromatics. [c] HTI: hydrogen transfer index ($C_4{}^0/C_4{}^=$).

for this investigation because of its longer catalytic lifespan and higher selectivity for light olefins.

The XRD patterns of the samples are displayed in Fig. S4.† It is clear that beta zeolites can be readily obtained when the HF/SiO_2 ratio is maintained at 0.35 or higher. The product compositions are listed in Table 3, which indicates that beta zeolites synthesized with different additions of HF have similar Si/Al ratios of about 280. The SEM images given in Fig. 1 show that sample B300-0.35, which was synthesized with relatively lower HF addition, consists of small and irregular crystalline particles. With the increasing HF/SiO_2 ratio, the products become larger, with sizes of about 2 to 3 μm, and adopt a more uniform morphology; this suggests that a higher HF dosage facilitates the crystallization and growth of the particles. Further magnification reveals that the crystal surfaces of all the samples grow in a less compact manner; they are rough, with many steps. The textural properties of the samples were measured by N_2 adsorption isotherms, and the results are summarized in Table 3. The samples synthesized with HF/SiO_2 ratios from 0.45 to 0.65 possess similar surface areas and pore volumes; sample B300-0.35 shows the largest BET surface area and external surface area, probably due to its irregular small particles. The NH_3-TPD curves are displayed in Fig. S5,† which reveals that beta zeolites synthesized with varied addition of HF possess similar profiles. However, there are obviously fewer acid sites on B300-0.35 than on beta synthesized with higher HF/SiO_2 ratios (Table 3), which is somewhat unexpected considering their similar Si/Al ratios.

Solid-state MAS NMR spectra were acquired to further investigate the local atomic environments in the samples. The ^{29}Si MAS NMR spectra of the calcined samples are displayed in Fig. 2(a). Four samples present similar spectra, with strong resonance lines at −111.6, −113.0 and −115.7 ppm; these are attributed to Si(4Si) species at different crystallographic sites.[46] Very weak signals corresponding to Si(3Si)(1Al) (possibly due to the presence of small amounts of Si(3Si)(1OH) species) can be discerned at −104 ppm due to the high Si/Al ratios of the samples. These spectra evidence the good framework connectivity of the samples.

The ^{27}Al spectra of the samples shown in Fig. 2(b) present two strong overlapping resonances between 50 and 65 ppm, attributed to tetrahedrally coordinated Al species.[47] The different peak shapes of the tetrahedral Al species among the samples imply a distinct Al distribution with varying HF addition.

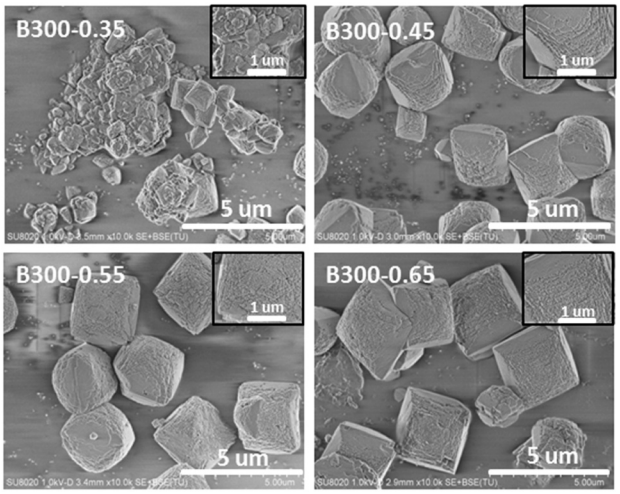

Fig. 1 SEM images of beta zeolites synthesized with different HF/SiO_2 ratios.

Moreover, a broad, weak resonance ranging from 0 to −20 ppm can be observed for all the samples; this becomes increasingly obvious with decreasing HF addition for the sample synthesis. This signal corresponds to extra-framework octahedral Al in very asymmetric and heterogeneous environments.[48,49] For sample B300-0.35, which was synthesized with the lowest HF dosage, an additional broad resonance centered around 15 ppm can be observed; this may also arise from distorted extra-framework octahedral Al species.[49] The higher amount of extra-framework Al species in sample B300-0.35 is consistent with its lower number of acid sites, as revealed by NH_3-TPD. The above results indicate that the HF dosage for the synthesis influences the stability of the Al species and the Al distribution in the products.

Given that the distribution of tetrahedral Al atoms in the framework determines their accessibility and affects the acidity and catalytic properties of the zeolites, the Al locations in high-Si beta were further investigated by ^{27}Al MQ MAS NMR. It should be noted that although the present high-Si beta samples are intergrowths of polymorphs A and B, the similarity of the T-site structures in the two polymorphs has been demonstrated in previous studies.[49–51] The ^{27}Al MQ MAS NMR spectra of samples B300-0.45 and B300-0.65 are displayed in Fig. 3 and S6,† respectively. According to the literature,[52] the representative four slices parallel to the F2 dimension of the MQ

Table 3 Product compositions, textual properties and acid densities of beta zeolites synthesized with different HF/SiO_2 ratios[a]

Sample	Si/Al[b]	Surface area ($m^2\ g^{-1}$)			Pore volume ($cm^3\ g^{-1}$)		D_{acid}[c] ($mmol\ g^{-1}$)
		S_{BET}	S_{micro}	S_{ext}	V_{micro}	V_{meso}	
B300-0.35	280	502	364	138	0.18	0.11	0.041
B300-0.45	282	471	373	98	0.18	0.10	0.051
B300-0.55	269	462	366	96	0.18	0.11	0.053
B300-0.65	278	459	374	85	0.19	0.08	0.052

[a] Initial gel molar composition: $SiO_2 : Al_2O_3 : TEAOH : HF : H_2O = 1 : 1/600 : 0.5 : n : 3$ (160 °C, 12 h). [b] Determined by XRF. [c] Acid density determined by NH_3-TPD.

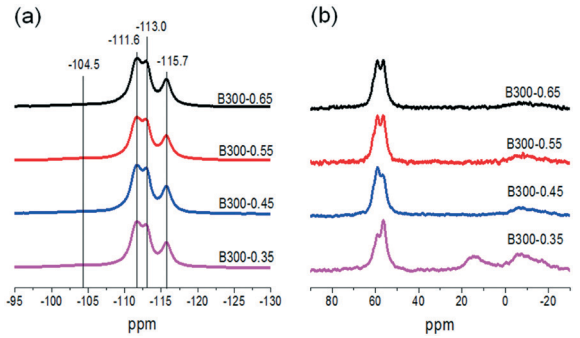

Fig. 2 ^{29}Si (a) and ^{27}Al MAS NMR spectra (b) of the calcined samples synthesized with different HF/SiO_2 ratios.

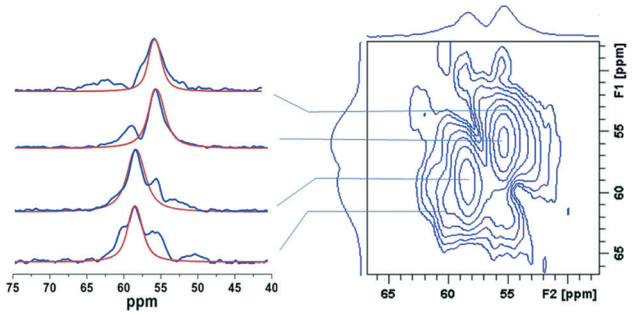

Fig. 3 ^{27}Al MQ MAS NMR spectrum of the calcined sample B300-0.45 (right) and the representative four slices (blue) parallel to the F2 dimension at selected F1 chemical shift positions with the fitted lines (red) (left).

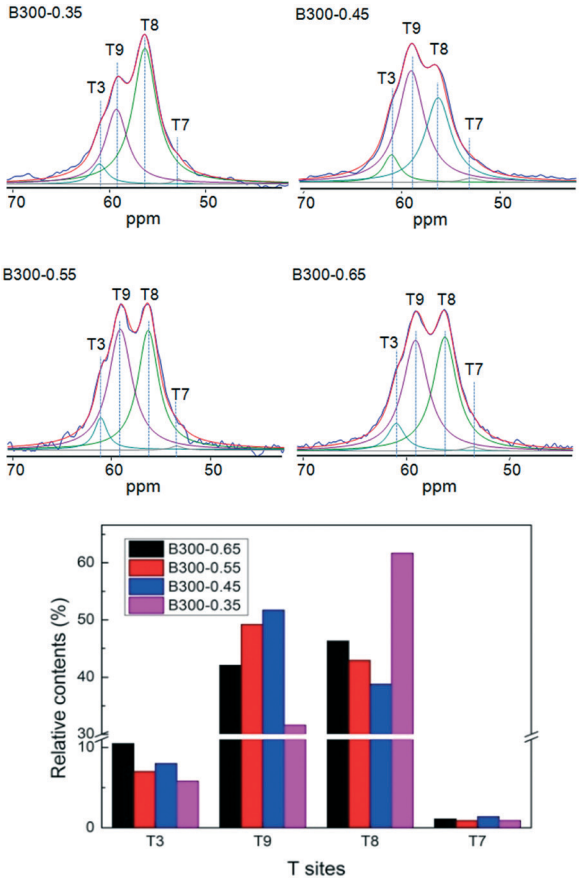

Fig. 4 ^{27}Al MAS NMR spectra with the deconvoluted peaks of the tetrahedral Al species (top) and the relative Al T-site occupancies (bottom) of the calcined high-Si beta zeolites. The blue and red lines represent the experimental and fitted spectra, respectively.

MAS NMR spectra at selected F1 chemical shift positions were extracted and then fitted to obtain the isotropic chemical shifts (δ_{iso}) and quadrupole interaction constants. As listed in Table S1,† the two samples show very similar results. Based on these parameters, the ^{27}Al MAS NMR spectra were fitted by the Q mass 1/2 method (Fig. 4), in which the different T sites are determined by the isotropic chemical shifts according to the DFT calculations reported by Lercher *et al.*[49] For a better comparison, the relative contents of tetrahedrally coordinated Al species are also summarized in Fig. 4. It is clear that the Al atoms mainly occupy four Al T sites (T3, T7, T8 and T9) in all the samples, despite the existence of nine crystallographically distinct T sites in the beta lattices. The major difference between the samples lies in the population of these T sites, especially at the T8 and T9 sites (the relative Al content of the T8 and T9 sites totals ~90%). Sample B300-0.45 possesses the highest relative content of T9 sites and the fewest T8 sites. The opposite case is observed for sample B300-0.35. From sample B300-0.45 to B300-0.65, the T9 sites content shows a gradual decrease, whereas the T8 sites content increases correspondingly. It should be noted that because the quantity of tetrahedral Al species in sample B300-0.35 is lower than that in other samples due to the existence of extra-framework Al, a comparison between the other three samples should be more reasonable.

3.3. Catalytic performance of high-Si beta synthesized with different HF/SiO_2 ratios in methanol conversion

Fig. 5 presents the methanol conversion and product distributions over high-Si beta synthesized with different HF/SiO_2 ratios. Sample B300-0.45 exhibits the longest catalytic lifetime; on this sample, methanol conversion over 99% can be maintained for 9.2 h. A gradual decrease of lifetime is observed for the samples synthesized with greater HF addition; sample B300-0.65 displays a short catalytic lifetime of 2.2 h. Because the three samples B300-0.45, B300-0.55 and B300-0.65 possess similar textural properties, acid densities, particle sizes and morphologies, the difference in their catalytic lifespans is speculated to be related to the different locations of their framework Al atoms as revealed by ^{27}Al MAS NMR. This is reasonable considering that the Al locations in the framework determine the acidity and microenvironment of the Brønsted acid sites, which can influence the formation/reaction of active intermediates and thus the catalytic performance. It is inferred that Al atoms located at T9 sites are favorable Al species for methanol conversion, which can result in longer catalytic stability of the catalyst. An extremely short lifetime was found for sample B300-0.35, which deactivated

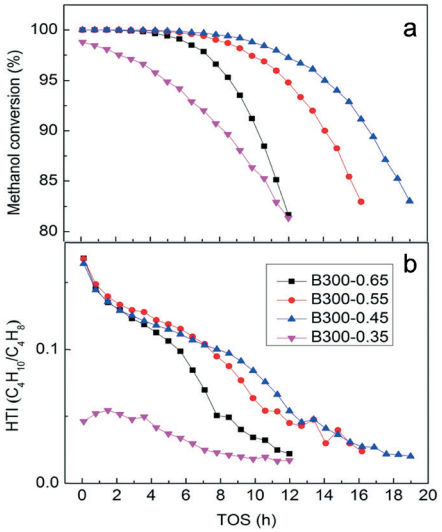

Fig. 5 Methanol conversion (a) and HTI values (b) as a function of time on stream over high-Si beta synthesized with different HF/SiO_2 ratios. Reaction conditions: 500 °C, WSHV = 4.0 h^{-1}.

after only several minutes of contact with methanol. Given that sample B300-0.35 has a large external surface area, which should facilitate mass transfer in the reaction, its unexpectedly poor catalytic stability should be related to its lower (insufficient) acid density and distinct Al distribution compared to the other samples. Indeed, the Al locations in samples B300-0.35 and B300-0.45 represent two extremes in the four samples, which is consistent with their catalytic stability performance. On the other hand, the existence of higher amounts of extra-framework Al in B300-0.35 may also have a negative effect on the reaction.

The product selectivities of the samples as a function of time on stream are shown in Fig. 6 and S7.† The four samples display similar evolution trends of product selectivity, with propene as the most abundant product, followed by butene and C_{5+}^N. At the beginning of the reaction, the selectivity to propene can reach ~50%; it shows a decreasing slope and decreases to ~47% before the occurrence of deactivation (99% conversion of methanol). Moreover, the selectivities towards ethene, aromatics and alkanes decrease gradually, whereas those of butene and C_{5+}^N increase with prolonged time on stream. The decreasing selectivities to C_1^0–C_4^0 alkanes and aromatics are in line with the decrease of HTI displayed in Fig. 5; they likely result from the loss (coverage) of catalytic sites and the decreased ability of the catalysts to facilitate some secondary reactions of olefin products, such as oligomerization, cyclization and hydrogen transfer. Fig. 6 also illustrates the detailed aromatic product distributions. It can be seen that bulky methylbenzenes with four, five and six methyl groups are the dominant aromatic species. As previous studies have revealed that higher methylbenzenes are the active intermediates over H-beta at relatively low reaction temperatures (*e.g.* 350 °C) and facilitate the formation of propene, butene and a small amount of ethene, herein, the aromatics cycle route likely occurs in the reaction at 500 °C and contributes to the resulting product selectivity.

The propene/ethene and C_{5+}^N/butene ratios of the samples as a function of time on stream are plotted and displayed in Fig. 7; both ratios present increasing slopes. This implies a slower rate of decrease of propene as compared to that of ethene and a faster rate of increase of C_{5+}^N as compared to that of butene with an increase in time on stream. Although it is difficult to discriminate the fractions at which the aromatics and olefins routes contribute to the reaction from the current product distributions, it is apparent that the cracking activity for the higher olefins involved in the olefins-based cycle weakens as the reaction proceeds.

Based on sample B300-0.45, the reaction conditions were optimized to better understand the reaction behavior over the high-Si beta catalysts; the results are listed in Table 4. The influence of the reaction temperature was first investigated by varying the temperature from 450 °C to 600 °C (WHSV = 4 h^{-1}). The catalytic lifespan shows a dramatic increase from 450 °C to 500 °C, achieves its maximum at 550 °C, and then undergoes a decrease when the temperature further increases to 600 °C. The distinct difference in lifespan between 450 °C and other temperatures will be discussed in the following section according to the retained materials in the catalysts. Meanwhile, the product distribution changes gradually with increasing temperature from 450 °C to 600 °C. The selectivities to butene and C_{5+}^N decrease, and the selectivities to ethene and propene show a corresponding increase. This can be explained by the enhanced cracking ability of the catalysts at higher temperature. On the other hand, the selectivity of aromatics decreases from 450 °C to 550 °C,

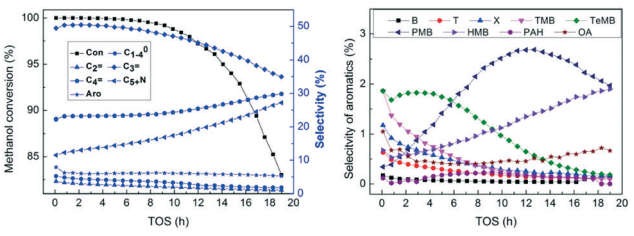

Fig. 6 Product selectivities (left) and detailed aromatic product distributions (right) as a function of time on stream over sample B300-0.45. Reaction conditions: 500 °C, WSHV = 4.0 h^{-1}. B: benzene, T: toluene, X: xylene, TMB: trimethylbenzene, TeMB: tetramethylbenzene, PMB: pentamethylbenzene, HMB: hexamethylbenzene, PAH: polycyclic aromatic hydrocarbon, OA: other aromatics.

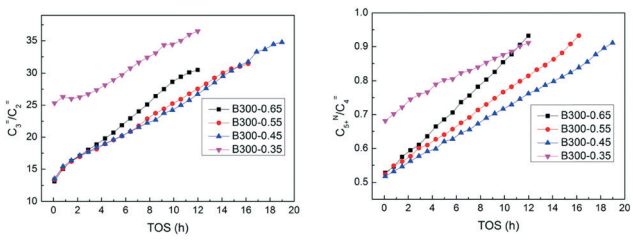

Fig. 7 C_3H_6/C_2H_4 ratio (left) and C_{5+}^N/C_4H_8 ratio (right) as a function of time on stream on high-Si beta synthesized with different HF/SiO_2 ratios. Reaction conditions: 500 °C, WSHV = 4.0 h^{-1}.

Table 4 Methanol conversion over sample B300-0.45 under different reaction conditions

Temperature (°C)	WSHV (h^{-1})	Lifetime[a] (h)	Selectivity[b] (wt%)							
			$C_{1-4}{}^{0}$	C_2H_4	C_3H_6	C_4H_8	$C_{5+}{}^{N}$	Aro	C_3H_6/C_2H_4	HTI
450	4	0.9	6.3	1.8	41.9	24.1	17.6	8.4	23.3	0.21
500	4	9.2	4.8	3.3	50.3	23.1	12.3	6.2	15.2	0.14
550	4	10.6	3.3	5.5	55.4	21.6	8.6	5.5	10.1	0.08
600	4	6.6	3.3	8.0	55.6	18.6	6.2	7.4	7.0	0.05
550	2	23.1	2.6	5.9	58.3	21.3	7.2	4.7	9.9	0.06

[a] Reaction duration with >99% methanol conversion. [b] Product selectivities at TOS = 47 min.

possibly due to the enhanced diffusion of olefin products. However, a further increase is observed at 600 °C, probably due to severe aromatization; this is consistent with the shortened catalytic lifespan.

The influence of weight space velocity on the reaction was investigated by decreasing the feed rate (WHSV = 2 h^{-1}). It was found that the selectivity to propene increases with decreasing selectivity to $C_{5+}{}^{N}$, which is probably due to enhanced cracking activity resulting from the prolonged feed-catalyst contact time. Meanwhile, the catalytic lifespan is significantly extended under a lower feed rate. As shown in Table 4 and Fig. S8,† a catalytic lifespan of 23.1 h with an initial propene selectivity of 58.3% can be achieved at 550 °C over B300-0.45. The corresponding initial propene/ethene ratio is 9.9. The propene selectivity and propene/ethene ratio change gradually and reach 49.7% and 16.4 before deactivation occurs. These results suggest that lower WHSV facilitates the catalytic efficiency of high-Si beta catalysts.

3.4. Retained coke species

The coke species retained in the B300-0.45 catalyst after reaction at 450 °C and 550 °C (WHSV = 4 h^{-1}) were analyzed by GC MS, and the results are given in Fig. 8. The coke content in the catalysts, shown in Fig. 8, was determined by TG (Fig. S9†) based on the weight loss between 300 °C and 650 °C. Only small amounts of aromatics (PMB and HMB) and phenol compounds and traces of long-chain hydrocarbons were detected on the used catalyst at 450 °C, which is consistent with its low coke content of 0.7 wt%. Note that phenols, which are unreported coke species, are basic molecules and have greater proton affinities than benzene. Han *et al.*[39] once identified an oxygen-containing compound, 4-methylbenzaldehyde, on used low-Si beta in the MTH reaction. They further revealed that oxygen-containing species such as 2-cyclopenten-1-one can block the Brønsted acid sites by strong chemisorption and convert rapidly to aromatics, which expedites the formation of coke and, thus, deactivation of the ZSM-5 catalyst.[53] Lercher *et al.*[54] also confirmed that rapid deactivation during the initial stage was caused by chemisorbed oxygen-containing species. Herein, considering that the small aromatics detected are usually taken as active reaction intermediates and cannot block the large pores of beta zeolite, it is speculated that the phenol species may adsorb strongly on the acid sites and cause rapid deactivation of the catalyst at 450 °C. Recently, Olsbye *et al.*[55] reported that diphenylmethane formation involves the dehydrogenation of methanol to formaldehyde, followed by subsequent reaction with two benzene molecules. A similar process may occur in the formation of 6,6′-methylenebis(2-*tert*-butyl)-3-methylphenol. A rough calculation shows that the used catalyst contains about 0.081 mmol g^{-1} phenols using C_2Cl_6 as an internal standard, which is higher than the acid density of sample B300-0.45 as measured by NH_3-TPD. The coke species generated at 550 °C are obviously more abundant than those at 450 °C. However, the coking rate at 550 °C (2.4 mg g^{-1} h^{-1}) is slower than that at 450 °C (7.8 mg g^{-1} h^{-1}); this may be due to enhanced product diffusion and cracking ability at higher temperatures. It is supposed that a higher reaction

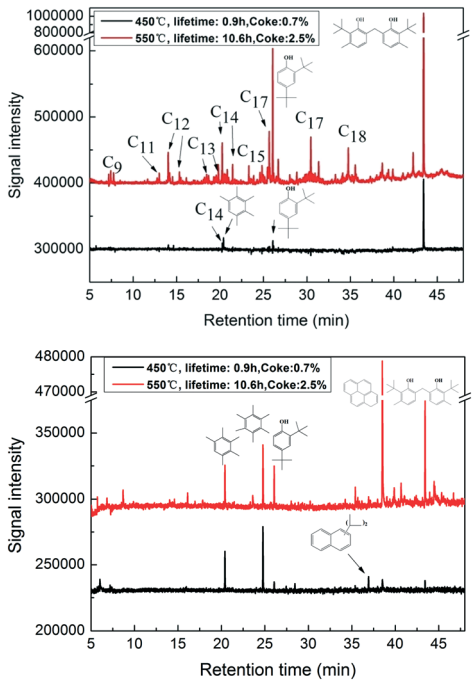

Fig. 8 GC-MS chromatograms of the organic species retained in the deactivated catalysts. The organic species were first extracted by dichloromethane (top) and then dissolved in 40% HF solution, followed by further dichloromethane extraction (bottom). The reaction was stopped once the methanol conversion was below 99%; the catalysts were then discharged and quenched by liquid nitrogen.

temperature weakens the adsorption of phenol compounds, which allows the catalyst to be active for a longer period and accommodates more coke before deactivation. Finally, the accumulated pyrene and long-chain hydrocarbons together with phenol compounds cause deactivation of the catalyst at 550 °C.

3.5. $^{12}C/^{13}C$-methanol switch experiments on high-Si beta at high temperature

$^{12}C/^{13}C$-methanol isotropic switch experiments are an effective method to study reaction mechanisms by distinguishing ^{13}C incorporation in the organic products. After switching from ^{12}C to ^{13}C-methanol, the organic reactive center is more active towards ^{13}C-methanol than the other species, and the corresponding effluent products contain more ^{13}C atoms.

Fig. 9 displays the ^{13}C content of the effluent olefins and methylbenzenes at 450 °C and 550 °C after 30 min of ^{12}C-methanol reaction followed by 30 s of ^{13}C-methanol reaction over high-Si beta B300-0.45. The ^{13}C content of the effluent olefins is higher than 90%, while the ^{13}C content of the effluent PMB and HMB, which have been proven to be the main HCP species on beta zeolite, is less than 10%. These results indicate that the olefins methylation and cracking mechanism is the dominant route for the generation of olefins over the present high-Si beta zeolites; also, PMB and HMB are almost inactive for methanol conversion to light olefins, likely due to their ready diffusion out of the large pores of beta zeolite. The higher ^{13}C content in the effluent X, TMB and TeMB at 450 °C suggests greater dominance of the hydrogen transfer reaction at 550 °C, possibly due to the reduced diffusion rate of olefin products at relatively low temperatures. This is consistent with the higher aromatics selectivity at 450 °C displayed in Table 4. These findings are different from previous reports for beta zeolites which involve both the aromatics-based cycle and the olefins-based cycle.[13,23,56] We propose that the low density of acid sites on catalyst B300-0.45 is the main factor responsible for the present reaction pathway.

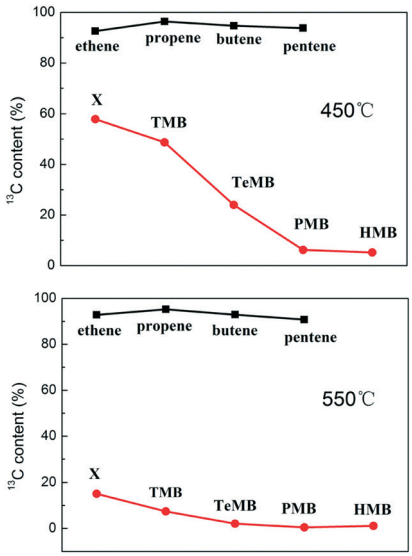

Fig. 9 ^{13}C content in the effluent olefins and methylbenzenes at 450 °C and 550 °C after 30 min of ^{12}C-methanol reaction followed by 30 s of ^{13}C-methanol reaction over high-Si beta B300-0.45. X: xylene, TMB: trimethylbenzene, TeMB: tetramethylbenzene, PMB: pentamethylbenzene, HMB: hexamethylbenzene.

In summary, the olefins-based cycle is dominant in the methanol reaction at high temperature over high-Si beta, which produces propene in high selectivity and a high propene/ethene ratio with a long catalytic lifespan. The formation pathway of ethene is distinct from most previous reports, in which the aromatics cycle is mainly responsible for its generation.[10,23,57] The low selectivity of ethene herein is possibly due to the slow rate of cracking of olefins to ethene.[58,59] Both the catalyst acidity and reaction temperature show great influence on the reaction behaviors, in which a low acid site concentration reduces the selectivity of aromatics and a high reaction temperature enhances the cracking ability of heavier olefins and facilitates product diffusion; these function together and result in catalysts with improved catalytic stability and high propene selectivity.

4. Conclusions

Large pore high-silica beta was demonstrated to be an effective catalyst for the MTP reaction. It was found that the density of acid sites, Al locations and reaction conditions have great influence on the catalytic performance. The lower acid density associated with high-silica beta suppresses the formation of aromatics, and a higher reaction temperature improves the cracking of heavier olefins and diffusion of the products, both of which facilitate the achievement of high propene selectivity. High-Si beta with abundant T9 site Al species demonstrated the longest catalytic lifespan, possibly due to the suitable acidity and microenvironment of the corresponding Brønsted acid sites. According to $^{12}C/^{13}C$-methanol switch experiments, the olefins-based mechanism is dominant in the reaction and contributes to the formation of ethene, propene and higher olefins. The present work suggests that despite the lack of space limitations, large pore zeolites with high Si/Al ratios can provide interesting catalytic performance in the MTP reaction if the acidity (Si/Al ratio) is carefully controlled. We expect that more large pore zeolites with low acid densities will be explored in the future, which will promote research into the mechanism of methanol conversion and catalyst development for the MTP process.

Conflicts of interest

There are no conflicts to declare.

Acknowledgements

This work was supported by the National Natural Science Foundation of China (21676262) and the Key Research Program of Frontier Sciences, CAS (QYZDB-SSW-JSC040).

Notes and references

1 Z. M. Liu, C. L. Sun, G. W. Wang, Q. X. Wang and G. Y. Cai, *Fuel Process. Technol.*, 2000, **62**, 161–172.
2 P. Tian, Y. Wei, M. Ye and Z. Liu, *ACS Catal.*, 2015, **5**, 1922–1938.
3 Z. M. Liu and J. Liang, *Curr. Opin. Solid State Mater. Sci.*, 1999, **4**, 80–84.
4 J. Q. Chen, B. V. Vora, P. R. Pujado, A. Gronvold, T. Fuglerud and S. Kvisle, *Stud. Surf. Sci. Catal.*, 2004, **147**, 1–6.
5 J. Q. Chen, A. Bozzano, B. Glover, T. Fuglerud and S. Kvisle, *Catal. Today*, 2005, **106**, 103–107.
6 H. Koempel and W. Liebner, *Stud. Surf. Sci. Catal.*, 2007, **167**, 261–267.
7 I. M. Dahl and S. Kolboe, *J. Catal.*, 1994, **149**, 458–464.
8 I. M. Dahl and S. Kolboe, *J. Catal.*, 1996, **161**, 304–309.
9 D. Lesthaeghe, A. Horre, M. Waroquier, G. B. Marin and V. Van Speybroeck, *Chem. – Eur. J.*, 2009, **15**, 10803–10808.
10 M. Bjørgen, S. Svelle, F. Joensen, J. Nerlov, S. Kolboe, F. Bonino, L. Palumbo, S. Bordiga and U. Olsbye, *J. Catal.*, 2007, **249**, 195–207.
11 S. Xu, A. Zheng, Y. Wei, J. Chen, J. Li, Y. Chu, M. Zhang, Q. Wang, Y. Zhou, J. Wang, F. Deng and Z. Liu, *Angew. Chem., Int. Ed.*, 2013, **52**, 11564–11568.
12 W. G. Song, H. Fu and J. F. Haw, *J. Am. Chem. Soc.*, 2001, **123**, 4749–4754.
13 S. Svelle, U. Olsbye, F. Joensen and M. Bjorgen, *J. Phys. Chem. C*, 2007, **111**, 17981–17984.
14 S. Svelle, F. Joensen, J. Nerlov, U. Olsbye, K.-P. Lillerud, S. Kolboe and M. Bjorgen, *J. Am. Chem. Soc.*, 2006, **128**, 14770–14771.
15 Y. V. Kissin, *Catal. Rev.: Sci. Eng.*, 2001, **43**, 85–146.
16 J. Li, Y. Wei, J. Chen, S. Xu, P. Tian, X. Yang, B. Li, J. Wang and Z. Liu, *ACS Catal.*, 2015, **5**, 661–665.
17 J. Chen, J. Li, Y. Wei, C. Yuan, B. Li, S. Xu, Y. Zhou, J. Wang, M. Zhang and Z. Liu, *Catal. Commun.*, 2014, **46**, 36–40.
18 J. Wang, J. Li, S. Xu, Y. Zhi, Y. Wei, Y. He, J. Chen, M. Zhang, Q. Wang, W. Zhang, X. Wu, X. Guo and Z. Liu, *Chin. J. Catal.*, 2015, **36**, 1392–1402.
19 J. Wang, Y. Wei, J. Li, S. Xu, W. Zhang, Y. He, J. Chen, M. Zhang, A. Zheng, F. Deng, X. Guo and Z. Liu, *Catal. Sci. Technol.*, 2016, **6**, 89–97.
20 W. Dai, M. Dyballa, G. Wu, L. Li, N. Guan and M. Hunger, *J. Phys. Chem. C*, 2015, **119**, 2637–2645.
21 X. Wang, W. Dai, G. Wu, L. Li, N. Guan and M. Hunger, *Catal. Sci. Technol.*, 2014, **4**, 688–696.
22 D. A. Simonetti, J. H. Ahn and E. Iglesia, *J. Catal.*, 2011, **277**, 173–195.
23 M. Bjørgen, F. Joensen, K.-P. Lillerud, U. Olsbye and S. Svelle, *Catal. Today*, 2009, **142**, 90–97.
24 M. Zhang, S. Xu, Y. Wei, J. Li, J. Chen, J. Wang, W. Zhang, S. Gao, X. Li, C. Wang and Z. Liu, *RSC Adv.*, 2016, **6**, 95855–95864.
25 C. D. Chang, C. T. W. Chu and R. F. Socha, *J. Catal.*, 1984, **86**, 289–296.
26 M. Westgard Erichsen, S. Svelle and U. Olsbye, *J. Catal.*, 2013, **298**, 94–101.
27 M. Westgard Erichsen, S. Svelle and U. Olsbye, *Catal. Today*, 2013, **215**, 216–223.
28 F. Bleken, M. Bjorgen, L. Palumbo, S. Bordiga, S. Svelle, K.-P. Lillerud and U. Olsbye, *Top. Catal.*, 2009, **52**, 218–228.
29 L. T. Yuen, S. I. Zones, T. V. Harris, E. J. Gallegos and A. Auroux, *Microporous Mater.*, 1994, **2**, 105–117.
30 J. F. Haw, W. G. Song, D. M. Marcus and J. B. Nicholas, *Acc. Chem. Res.*, 2003, **36**, 317–326.
31 W. Dai, N. Li, L. Li, N. Guan and M. Hunger, *Catal. Commun.*, 2011, **16**, 124–127.
32 J. Chen, J. Li, C. Yuan, S. Xu, Y. Wei, Q. Wang, Y. Zhou, J. Wang, M. Zhang, Y. He, S. Xu and Z. Liu, *Catal. Sci. Technol.*, 2014, **4**, 3268–3277.
33 W. Dai, X. Wang, G. Wu, L. Li, N. Guan and M. Hunger, *ChemCatChem*, 2012, **4**, 1428–1435.
34 S. Ivanova, C. Lebrun, E. Vanhaecke, C. Pham-Huu and B. Louis, *J. Catal.*, 2009, **265**, 1–7.
35 M. Firoozi, M. Baghalha and M. Asadi, *Catal. Commun.*, 2009, **10**, 1582–1585.
36 C. Mei, P. Wen, Z. Liu, H. Liu, Y. Wang, W. Yang, Z. Xie, W. Hua and Z. Gao, *J. Catal.*, 2008, **258**, 243–249.
37 M. Yoshioka, T. Yokoi and T. Tatsumi, *ACS Catal.*, 2015, **5**, 4268–4275.
38 M. Niwa and N. Katada, *Chem. Rec.*, 2013, **13**, 432–455.
39 Z. Liu, X. Dong, Y. Zhu, A.-H. Emwas, D. Zhang, Q. Tian and Y. Han, *ACS Catal.*, 2015, **5**, 5837–5845.
40 O. Mikkelsen and S. Kolboe, *Microporous Mesoporous Mater.*, 1999, **29**, 173–184.
41 M. Zhang, S. Xu, J. Li, Y. Wei, Y. Gong, Y. Chu, A. Zheng, J. Wang, W. Zhang, X. Wu, F. Deng and Z. Liu, *J. Catal.*, 2016, **335**, 47–57.
42 J. Zhang, Z. Huang, P. Li, X. Zhang, X. Zhang, Y. Yuan and L. Xu, *Catal. Sci. Technol.*, 2017, **7**, 2194–2203.
43 R. Otomo, U. Mueller, M. Feyen, B. Yilmaz, X. Meng, F.-S. Xiao, H. Gies, X. Bao, W. Zhang, D. De Vosh and T. Yokoi, *Catal. Sci. Technol.*, 2016, **6**, 713–721.
44 J. Rocha, C. M. Morais and C. Fernandez, *Top. Curr. Chem.*, 2005, **246**, 141–194.
45 A. Medek, J. S. Harwood and L. Frydman, *J. Am. Chem. Soc.*, 1995, **117**, 12779–12787.
46 M. E. Smith and E. R. H. van Eck, *Prog. Nucl. Magn. Reson. Spectrosc.*, 1999, **34**, 159–201.
47 J. Perezpariente, J. Sanz, V. Fornes and A. Corma, *J. Catal.*, 1990, **124**, 217–223.
48 S. M. Maier, A. Jentys and J. A. Lercher, *J. Phys. Chem. C*, 2011, **115**, 8005–8013.
49 A. Vjunov, J. L. Fulton, T. Huthwelker, S. Pin, D. Mei, G. K. Schenter, N. Govind, D. M. Camaioni, J. Z. Hu and J. A. Lercher, *J. Am. Chem. Soc.*, 2014, **136**, 8296–8306.
50 M. M. Martinez-Inesta, I. Peral, T. Proffen and R. F. Lobo, *Microporous Mesoporous Mater.*, 2005, **77**, 55–66.
51 C. A. Fyfe, H. Strobl, G. T. Kokotailo, C. T. Pasztor, G. E. Barlow and S. Bradley, *Zeolites*, 1988, **8**, 132–136.
52 J. Z. Hu, C. Wan, A. Vjunov, M. Wang, Z. Zhao, M. Y. Hu, D. M. Camaioni and J. A. Lercher, *J. Phys. Chem. C*, 2017, **121**, 12849–12854.

53 Z. Liu, X. Dong, X. Liu and Y. Han, *Catal. Sci. Technol.*, 2016, **6**, 8157–8165.
54 S. Mueller, Y. Liu, M. Vishnuvarthan, X. Sun, A. C. van Veen, G. L. Haller, M. Sanchez-Sanchez and J. A. Lercher, *J. Catal.*, 2015, **325**, 48–59.
55 J. S. Martinez-Espin, K. De Wispelaere, M. W. Erichsen, S. Svelle, T. V. W. Janssens, V. Van Speybroeck, P. Beato and U. Olsbye, *J. Catal.*, 2017, **349**, 136–148.
56 M. Bjorgen, U. Olsbye, D. Petersen and S. Kolboe, *J. Catal.*, 2004, **221**, 1–10.
57 B. P. C. Hereijgers, F. Bleken, M. H. Nilsen, S. Svelle, K.-P. Lillerud, M. Bjorgen, B. M. Weckhuysen and U. Olsbye, *J. Catal.*, 2009, **264**, 77–87.
58 S. Svelle, P. O. Ronning, U. Olsbye and S. Kolboe, *J. Catal.*, 2005, **234**, 385–400.
59 S. Svelle, P. A. Ronning and S. Kolboe, *J. Catal.*, 2004, **224**, 115–123.

